Check for updates

OPEN

Photocatalytic degradation of industrial acrylonitrile wastewater by F–S–Bi–TiO$_2$ catalyst of ultrafine nanoparticles dispersed with SiO$_2$ under natural sunlight

Feng Ouyang[1,2]✉, Hanliang Li[2,6], Zhengya Gong[2], Dandan Pang[3,6], Lu Qiu[2,4]✉, Yun Wang[2], Fangwei Dai[2], Gang Cao[5] & Bandna Bharti[2]

Highly active photocatalyst, having certain anti-ionic interfering function, of F, S and Bi doped TiO$_2$/SiO$_2$ was used for the first time to degrade the organic pollutants in acrylonitrile industrial wastewater under natural sunlight. The photocatalyst were prepared and characterized by UV–Vis, XRD, TEM, EDS, Nitrogen physical adsorption and XPS technique. UV–Vis analysis revealed addition of F, S and Bi into the lattice of TiO$_2$ led to the expansion of TiO$_2$ response in the visible region and hence the efficient separation of charge carrier. The photocatalytic potential of as prepared catalyst to degrade acrylonitrile wastewater under simulated and natural sunlight irradiation was investigated. The extent of degradation of acrylonitrile wastewater was evaluated by chemical oxygen demand (COD$_{Cr}$). COD$_{Cr}$ in wastewater decreased from 88.36 to 7.20 mgL^{-1} via 14 h irradiation of simulated sunlight and achieved regulation discharge by 6 h under natural sunlight, illuminating our photocatalyst effectiveness for refractory industrial wastewater treatment. From TEM results, we found that SiO$_2$ could disperse the photocatalyst with different component distributions between the surface and the bulk phase that should also be responsible for the light absorption and excellent photocatalytic performance. The XPS analysis confirmed the presence of surface hydroxyl group, oxygen vacancies.

Acrylonitrile is considered as a significant industrial chemical, originated by the direct oxidation of propylene with ammonia. It is extensively used for the preparation of synthetic rubber and resin, plastic and acrylic fiber[1,2]. Various types of organic pollutants are formed during the production of acrylonitrile[3,4] which has definitely induced serious impact on environmental and public health. Owing to its low bioavailability, high toxicity and mingled composition, acrylonitrile production wastewater has been directed as one type of refractory organic wastewater[5]. Therefore, it is necessary to develop a safe and efficient technology for the treatment of acrylonitrile wastewater. Various methods have been reported for the treatment of acrylonitrile wastewater, among those methods photocatalysis acquired much attention over the past decade. Since, photocatalytic reaction under sunlight irradiation is more energy-advantageous, and a lot of researchers have made vast efforts to realize the industrialization of photocatalytic treatment of industrial wastewater under sunlight[6–8]. However, there were few successful reports under sunlight because of the complexity of industrial wastewater[9–11]. Thus, photocatalytic

[1]State Key Laboratory of Urban Water Resource and Environment, Harbin Institute of Technology, Harbin 150090, People's Republic of China. [2]School of Civil and Environmental Engineering, Harbin Institute of Technology, Shenzhen 518055, People's Republic of China. [3]Henan University of Urban Construction, Pingdingshan 467036, People's Republic of China. [4]Tonson Tech Automation Equipment CO., Ltd, Shenzhen 518100, People's Republic of China. [5]Shenzhen Key Laboratory of Organic Pollution Prevention and Control, Harbin Institute of Technology, Harbin, People's Republic of China. [6]These authors contributed equally: Hanliang Li and Dandan Pang. ✉email: ouyangfh@hit.edu.cn; 329967681@qq.com

treatment of industrial wastewater under sunlight was a great challenge for the researchers. Watanabe[12] have reported that photocatalysis would cause a new environment revolution twenty years ago.

It is well known that, semiconductor-based photocatalysts have been investigated as an auspicious material for the solar energy conversion in regard to the breakdown of hazardous organic pollutants[13]. Across various photocatalysts, titanium dioxide (TiO_2) is known as the most determined material because of its chemical stability, high oxidation potential, nontoxicity and physical stability[14]. However, the use of TiO_2 in photocatalysis are limited because of its certain drawbacks like: their large band gap[15], which means that in solar energy processes, only UV light can be utilized and their low photocatalytic efficiency because of the fast recombination rate of electron–hole pairs. Therefore, many efforts have been promoted to reduce the bandgap of TiO_2 by doping or by band gap engineering[12–19]. In our previous study, the high photocatalytic activity of F-doped TiO_2 was attributed to the increase in the number and strength of surface acid sites[20]. It was explained that F-doping led to the creation of surface oxygen vacancies[17], or the increase of Ti^{3+} state[21]. On the other hand, higher photocatalytic activity of S doped sample was attributed to the increase in the surface Bronsted and Lewis acid sites[22]. Samantaray indicated that sulphate radical impregnation decreases the crystallite size and stabilized the anatase phase of TiO_2[23]. In addition, Bi doped TiO_2 exhibited a red shift in the optical adsorption and $Bi^{3+\delta+}$ species played a vital role in minimizing the electron hole recombination[16]. According to Li et al.[24], Bi doping into TiO_2 generates a new intermediate energy level below the conduction band edge of TiO_2, extending the absorption in the visible region and enhanced their photocatalytic efficiency. On the other hand, SiO_2 was used usually as a supporter, and its dispersing effect on nanoparticle size as well as that with oxidativity has not been reported.

To improve the photocatalytic activity of TiO_2 for the decomposition of organic pollutants in acrylonitrile wastewater under solar light irriadiation, we modified TiO_2 with the combination of silica and F, S, Bi doping (F–S–Bi–TiO_2/SiO_2). The dispersion of SiO_2 produced ultrafine nanoparticles. We have found that silica dispersion changed the aggregation state, constituent distribution in amount and morphology of the nanocatalyst, which was responsible for light absorption and increased photocatalytic activity[20]. We first degraded the acrylonitrile simulated wastewater and then degraded the acrylonitrile wastewater. This photocatalyst exhibited excellent performances in both the photocatalytic decompositions of organic pollutants under simulated and natural sunlight. So, our approach is an important attempt for the photocatalytic treatment of industrial wastewater.

Characterization

The valence states on the surface of catalysts were analyzed by a Thermo ESCALAB 250XI X-ray photoelectron spectrometer (America) using Al Kα (hn = 1,486.6 eV) as a radiation source. The irradiation of simulated sunlight and natural sunlight intensity was measured with a FZ-A RADIOMETER irradiance meter (China). From 6 am–8 pm, it was measured at a certain interval as shown in Table S1. Tecnai G^2 F30 TEM was used to analyze the physical structural characteristics of the photocatalysts. The samples were ultrasonically dispersed in ethanol. The suspension was deposited on a Lacey-carbon film, which was supported on a copper grid. The particle size distributions of catalysts with or without SiO_2 dispersant were calculated with NIH software using TEM image treatment. The crystalline phases of the photocatalysts were determined by X-ray diffractometer (RIGAKU, D/Max 2500PC, Japan) at a scanning rate of 6° min^{-1} in the 2θ angle range of 10°–80° using Cu Kα radiation combined with nickel filter. The accelerating voltage and the applied current were 40 kV and 200 mA, respectively. Crystallite sizes were calculated according to Scherrer equation:

$$L = K\lambda/B\cos\theta, \quad B^2 = B_{mea}^2 - b_{ins}^2 \tag{1}$$

where L, K, λ and θ are the average crystal size, the shape factor for spherical crystallites, the X-ray wavelength and Bragg diffraction angle, respectively. B, B_{mea} and b_{ins} are the breadths of intrinsic diffraction profile, the test sample diffraction integral profile and instrumental diffraction profile, respectively. UV–visible spectra were measured on UV-2450 UV spectrophotometer (Shimadzu Corporation, Japan). The range of the scanning wavelength was 200–800 nm. The BET specific surface area was measured by BELSOROP-MINI II (Japan) adsorption instrument and pore size distribution was analyzed by Barrett–Joyner–Halenda (BJH) method.

GC–MS (Agilent 7890A-5795C, America) was used for the component's analysis. The instrument was equipped with a DB-5 capillary column (length of 30 m, 0.25 mm i.d., 0.25 mm d.f.). The injector and MS transmission line temperatures were 250 and 310 °C, respectively. The oven temperature initiated at 40 °C (hold for 5 min), and then increased at 5 °C min^{-1} to 290 °C (hold for 2 min). The electron energy was set at 70 eV and the ion source temperature was 230 °C. The standard spectra in GC–MS database was used to identify the chemical constituents in wastewater. In the present study, refractory acrylonitrile wastewater was obtained from an acrylonitrile manufacturing plant. The acrylonitrile wastewater was pretreated through adsorption with microporous zeolite, HZSM-5 before photocatalytic degradation, COD_{Cr} decreased from 582.4 to 88.36 mgL^{-1}, and after that there were no change in the values. The organic pollutants in the wastewater after adsorption were detected and the results were listed in Table 1.

Photocatalytic activities for acrylonitrile simulated wastewater.

The photocatalytic activities of the photocatalyst used for acrylonitrile simulated wastewater were evaluated in a photocatalytic reaction system[20]. The quartz glass reactor was sealed after 180 mL of acrylonitrile wastewater (10 mgL^{-1}) and 300 mg of the catalyst was placed in it. The mixture was magnetically stirred in the dark until the adsorption equilibrium attained. Then, the spherical Xenon short arc lamp (AHD350, 350 W) was turned on for 12 min. In the process of illumination, the reaction solution of 1 mL was taken out at the interval of 2 min, and after that photocatalyst was filtered out through a filter film of 0.45 μm, acrylonitrile concentration was measured by HP-LC with LC-2030 UV detector and Sunfire TM C18 column. The wavelength of detector was 210 nm and the mobile phase volume ratio of methanol to water was 3:7. Triplicate samples from each batch were taken for the tests.
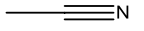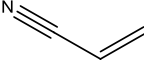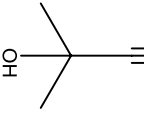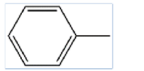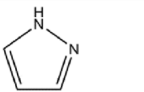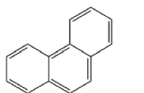
S. no	Primary pollutants	Structural formula	Concentration (mgL^{-1})	
			Raw water	HZSM-5
1	Acetonitrile		10.45	2.24
2	Acrylonitrile		23.10	4.65
3	Acetone cyanohydrin		420.98	54.35
4	Toluene		10.56	3.14
5	Pyrazole		8.37	5.83
6	Phenanthrene		6.45	2.79

Table 1. The main organic pollutants in the industrial acrylonitrile wastewater after adsorption by HZSM-5.

Inorganic ions/COD$_{Cr}$/BOD	Inorganic ion concentrations (mgL^{-1})	
	Raw water	HZSM-5
Phosphate	0.06	0.03
Nitrate	1.38	1.06
Sulphate	189	61.8
Chloride ion	44	22
Fluorine ion	0.17	0.16
Calcium ion	2.92	1.13
Ferric ion	0.17	0.055
Cyanide	0.017	0.011
COD$_{Cr}$	582.4	88.36
BOD	1.15	2.24

Table 2. Concentration of inorganic ions, BOD and COD$_{Cr}$ in acrylonitrile raw wastewater and the wastewater after adsorption by HZSM-5.

The ion effects on photocatalytic activities of acrylonitrile simulated wastewater. The ion effects were examined by following procedure: appropriate amount of sodium sulfate and sodium chloride were added to 180 mL of solution to obtain 61.8 mgL^{-1} of sulfate radical and 22 mgL^{-1} of chloride ion consistent with Table 2. The ion solution containing acrylonitrile was used for the comparative trial.

Activity evaluation by COD$_{Cr}$ and TOC measurements for acrylonitrile wastewater after adsorbed by HZSM-5. The catalyst contents and reaction device were used as the same as that in simulated wastewater. After adsorption equilibrium, the spherical Xenon lamp was turned on for 14 h. At given intervals of illumination, 4 mL of reaction solution was taken out and was filtered out through a filter film of 0.45 μm (all detection procedures in this study were performed according to or as per China national standard except for special mention). COD$_{Cr}$ values were detected with a Fast COD Detection Instrument (LH-5B-3B(V8)). TOC concentrations of the samples were measured via a Shimadzu TOC analyzer (TOC-L CPN, Japan). Concentration of inorganic ions, BOD and COD$_{Cr}$ in acrylonitrile raw wastewater, the wastewater after adsorption measured according to national standard methods were listed in Table 2.
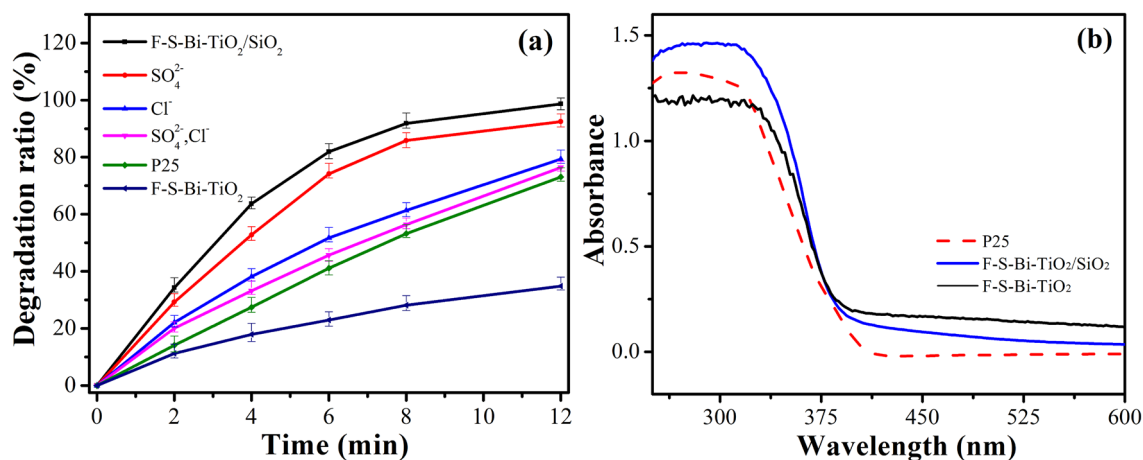
Figure 1.. (**a**) Photocatalytic activities of acrylonitrile simulated wastewater degradation of SO_4^{2-}, Cl^-, TiO_2–P25, F–S–Bi–TiO_2, and F–S–Bi–TiO_2/SiO_2; (**b**) UV–visible spectra of TiO_2–P25, F–S–Bi–TiO_2/SiO_2 and F–S–Bi–TiO_2.

Components	F–S–Bi–TiO_2	F–S–Bi–TiO_2/SiO_2
Average crystal size (nm)	40.4	13.9
Specific surface area (m^2/g)	45.9	194.3
Average pore diameter (nm)	26.0	14.1

Table 3. The average crystal size, specific surface area and average pore diameter of F–S–Bi–TiO_2 and F–S–Bi–TiO_2/SiO_2 samples.

Results

Effect of different ions on the activity and light adsorption performance.
Figure 1a shows the photocatalytic performances of the prepared samples for acrylonitrile simulated wastewater under the effect of spherical Xenon short arc lamp. The degradation ratio of F–S–Bi–TiO_2/SiO_2 catalyst after 4 min was 63%, which was much higher than TiO_2–P25 and F–S–Bi–TiO_2.

In order to demonstrate the interference of inorganic ions, a certain amounts of sodium sulfate (61.8 mgL^{-1} sulfate radical) and sodium chloride (22 mgL^{-1} chloride ion) were added into acrylonitrile simulated wastewater and the degradation was carried out by the catalyst under the same condition mentioned above. These results revealed that free sulfate radical, chloride ions, or sodium ions inhibited the degradation progress. This was similar with our previous studies which illustrated that, certain inhibition effect by free sulfate radical on the degradation process[22].

Figure 1b shows the UV–Visible spectra of TiO_2 P-25 (Degussa), F–S–Bi–TiO_2/SiO_2 and F–S–Bi–TiO_2 catalysts. The absorption of F–S–Bi–TiO_2/SiO_2 catalyst was increased in the UV–visible region at 300–600 nm as compared to TiO_2 P-25. However, the UV–visible spectrum of F–S–Bi–TiO_2 became flat below 335 nm, showing weakest absorbance. Although, F–S–Bi–TiO_2/SiO_2 exhibited lower absorption ability towards visible region (400–600 nm) than F–S–Bi–TiO_2, showing the higher degradation ratio. The higher degradation ratio was attributed to the better dispersion of SiO_2, because in F–S–Bi–TiO_2/SiO_2 photocatalyst TiO_2 was well dispersed, reducing the agglomeration and enhancing the absorption in the UV region[22]. However, both the photocatalysts have the same weight but F–S–Bi–TiO_2 contains more S elements and absorbed more visible light. The Photocatalytic reaction mainly depends upon the UV light.

XRD analysis.
In order to know the crystal structure of the prepared catalyst, XRD patterns of F–S–Bi–TiO_2/SiO_2 and F–S–Bi–TiO_2 calcinated at 450 °C were recorded as shown in Fig. S2. The crystallite size of the catalysts was calculated with the most predominant peak of the anatase face (101) with the help of Scherrer equation (Table 3). It was clearly revealed from Table 3 that the addition of SiO_2 as a dispersant agent decreases the average crystal size, and increases the surface area of the photocatalyst.

TEM and EDS analysis.
The TEM images of as prepared photocatalyst without SiO_2 were shown in Fig. 2a–c. From Fig. 2a, we observed the crystal with grains size of 11–60 nm, and they might be formed in different aggregated stages. Aggregation of ca. 4 nm of particles were produced on the rough end faces, where borderline disappeared in the interior of the large piece crystal (Fig. 2b). The other type gave out indistinct borderline in Fig. 2c. The crystallite faces of TiO_2 ($d=0.356$ nm, (101)) and $Bi_4Ti_3O_{12}$ ($d=0.364$ nm, (009)) were exhibited in Fig. 2b,c. Package morphology has been identified clearly by TEM images (Fig. 2d). The atoms are arranged
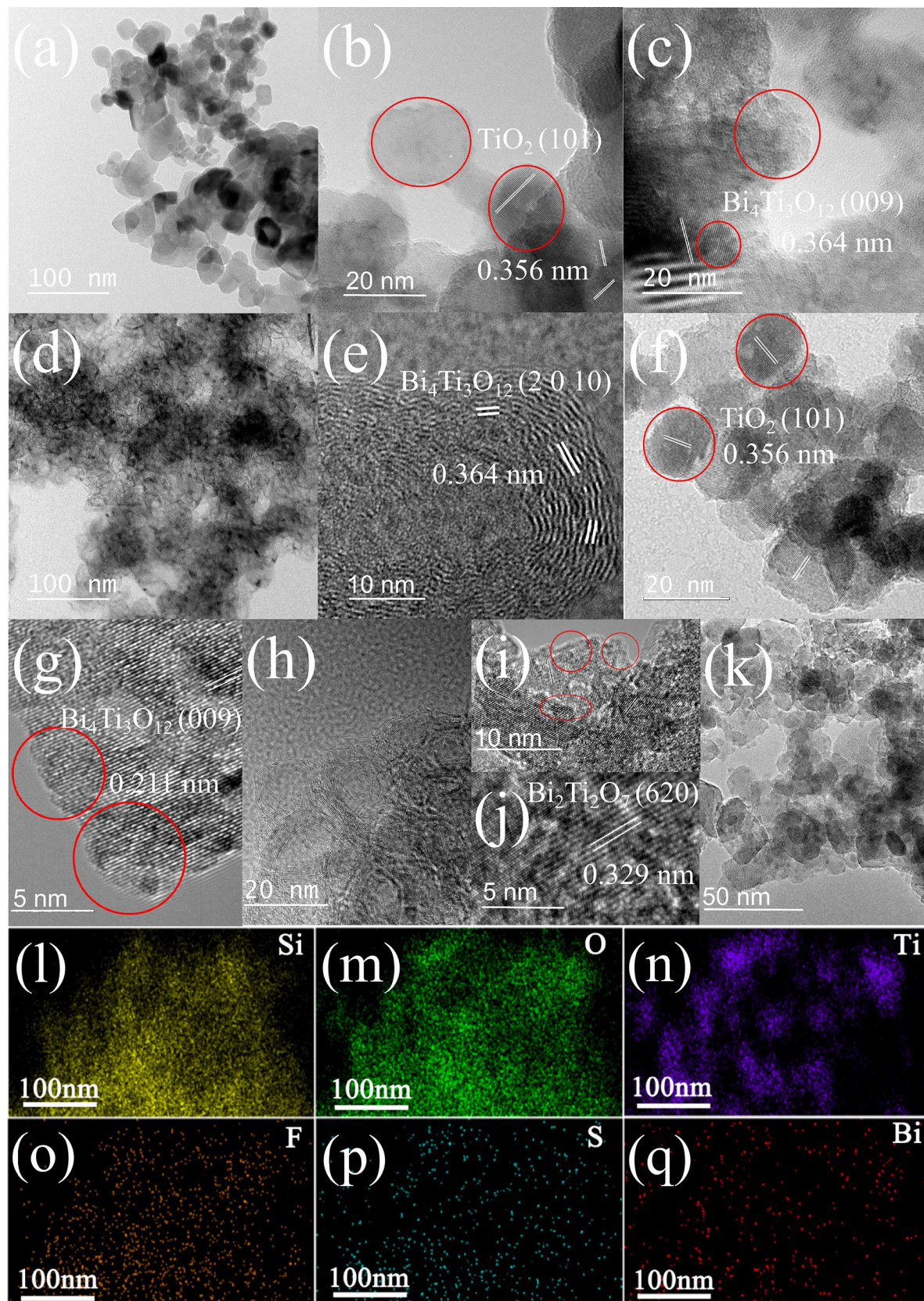
Figure 2.. TEM images of, (**a–c**) F–S–Bi–TiO$_2$ and (**d–k**) F–S–Bi–TiO$_2$/SiO$_2$ samples. (**l–q**) EDS mapping of Si, O, Ti, F, S and Bi elements of S–Bi–F–TiO$_2$/SiO$_2$ samples.
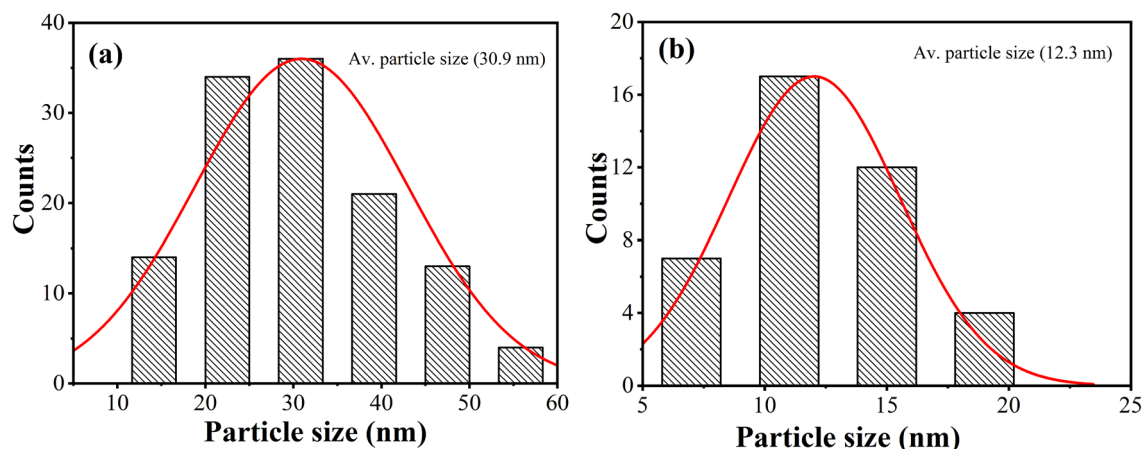
Figure 3.. Particle size distributions of (**a**) F–S–Bi–TiO$_2$ and (**b**) F–S–Bi–TiO$_2$/SiO$_2$ samples.

on irregular crystal planes of several nanometers of out layer films. The core surface was most rough (Fig. 2e). The package morphology was formed after the addition of SiO$_2$. The black parts in the figure represented the pores in SiO$_2$. The other general crystal configurations look like bulk type of TiO$_2$ and Bi$_4$Ti$_3$O$_{12}$ (Fig. 2f,g). As comparison to Fig. 2b, TiO$_2$ crystal with SiO$_2$ was also constituted by smaller particles of 2–4 nm with identical crystal face (Fig. 2f). Bi$_4$Ti$_3$O$_{12}$ (d = 0.211 nm, (2010)) crystal with borderline mark aggregated into a large crystal and also possessed identical crystal face (Fig. 2g). The explanation was that crystal growth might influence each other in same aggregate through the interface, connected among gel particles to form relatively larger identical crystal face, like as biomimetic crystallization. Based on the same principle of interaction of end face atoms, different crystal faces were developed at starting on an end face on the basis of total lowest-energy rule of the system (Fig. 2i). Bi$_2$Ti$_2$O$_7$ in Fig. 2j was regarded as the intermediate phase of Bi$_4$Ti$_3$O$_{12}$ formation[25]. A large number of bumps were also formed on the rough surfaces (Fig. 2k). The packages were formed by silk ribbon-like film twining (Fig. 2h). This film could be consisting of long identical crystal face and generated from stirring drawing. Relatively large mass of SiO$_2$ promoted drawing in late stage of gelation. The EDS images in Fig. 2 show that Si, O, Ti, F, S and Bi elements were evenly distributed on the surface of S–Bi–F–TiO$_2$/SiO$_2$ catalyst[26], which confirmed the conjecture that the elements were not detected in XRD.

The particle size distribution of the catalyst was calculated with NIH software for all particles in random region and was shown in Fig. 3. The catalyst without SiO$_2$ showed a wide particle size distribution. The average diameter was 30.9 nm, which was smaller than crystal grain size (40.4 nm) as calculated by XRD (Table 3). Since the borderline was not identified by the program, we measured the diameters of particles artificially and calculated particle size distribution of the catalyst with SiO$_2$ on the basis of the same rule. The result was shown in Fig. 3b. It has been found that the average diameter of the particles is 12.3 nm, which was in agreement with the XRD result (13.9 nm). Compared to the catalyst without SiO$_2$, nanoparticles sizes are apparently different. Nanoparticles sizes of the major parts were above *ca,* 20 nm for the catalyst without SiO$_2$, contrarily, they were below 16 nm for the catalyst with SiO$_2$ and the major parts belonged to ultrafine nanoparticles[27].

Nitrogen physical adsorption. Figure 4 represents the nitrogen adsorption and desorption isotherms of F–S–Bi–TiO$_2$/SiO$_2$ and F–S–Bi–TiO$_2$ calcined at 450 °C. Both F–S–Bi–TiO$_2$/SiO$_2$ and F–S–Bi–TiO$_2$ display type IV isotherm and H$_2$ hysteresis, which indicate the presence of mesoporous materials.

Moreover, the F–S–Bi–TiO$_2$/SiO$_2$ sample has the similar pore structure with F–S–Bi–TiO$_2$. The inset in Fig. 4 shows the plot for the pore size distribution determined by Barrett–Joyner–Halenda (BJH) method from the adsorption branch of the isotherm. The average pore diameters and total pore volume of F–S–Bi–TiO$_2$ were 26.0 nm, 0.30 cm^3/g and for F–S–Bi–TiO$_2$/SiO$_2$ are 14.1 nm, 0.67 cm^3/g. Both of them exhibit mesopore rich structure. However, at all pressure region, the adsorption amount of N$_2$ on F–S–Bi–TiO$_2$/SiO$_2$ was higher than that of F–S–Bi–TiO$_2$, which indicates that a lot of relatively small mesoporous on the surface of F–S–Bi–TiO$_2$/SiO$_2$ were formed under the action of SiO$_2$. Therefore, the specific surface area of F–S–Bi–TiO$_2$/SiO$_2$ (194.3 m^2/g) was higher than that of F–S–Bi–TiO$_2$ (45.9 m^2/g). And, greater adsorption capacity will lead to greater degradation rate, which was consistent with the experimental results.

XPS analysis. XPS spectra of F–S–Bi–TiO$_2$/SiO$_2$ and F–S–Bi–TiO$_2$ were shown in Fig. 5. Since fluorine doping converted Ti^{4+} state to Ti^{3+}, and these Ti^{3+} state was related to oxygen vacancies[28], the content of F changes in both types of the catalysts were investigated. In Fig. 5a the F 1s spectrum of F–S–Bi–TiO$_2$ shows only one peak centered at binding energy 684.4 eV (represented by red color), indicated only surface fluoride species were present in F–S–Bi–TiO$_2$. However, in case of F–S–Bi–TiO$_2$/SiO$_2$, the F 1s XPS spectra shows two peaks centered at binding energy 688.5 and 686.2 eV, respectively (represented by black color). The peak at binding energy 688.5 eV was attributed to the doped F into the substituted sites of TiO$_2$ lattice and produced mixed oxide structure of O–Ti–F[18,29,30]. The lower binding energy, centered at 686.2 eV was attributed to the surface fluoride species adsorbed on the surface of TiO$_2$[30]. This result shows that silica plays a very important role in stabiliz-
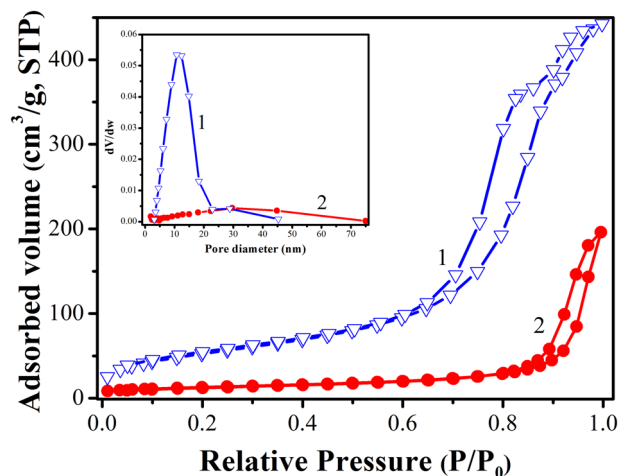
Figure 4.. Nitrogen adsorption and desorption isotherms of (**1**) F–S–Bi–TiO$_2$/SiO$_2$ and (**2**) F–S–Bi–TiO$_2$. Inset shows BJH pore size distributions of the corresponding samples.
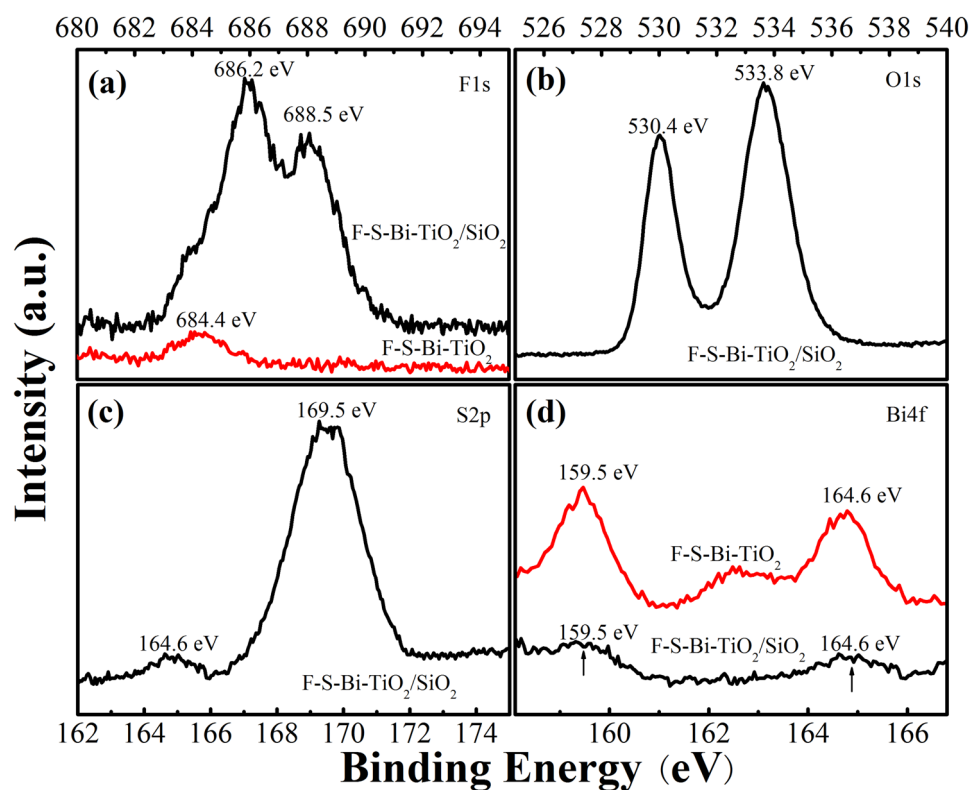
Figure 5.. XPS spectra of F–S–Bi–TiO$_2$ and F–S–Bi–TiO$_2$/SiO$_2$ samples: (**a**) F 1s spectra; (**b**) O 1s spectrum; (**c**) S 2p spectrum; (**d**) Bi 4f spectra.

ing the dispersion of F ions. Next, the O 1s spectrum of F–S–Bi–TiO$_2$/SiO$_2$ catalyst was shown in Fig. 5b. The peak at binding energy 533.8 eV was attributed to oxygen present in surface hydroxyl species[29], while the peak at binding energy 530.4 eV ascribed to lattice oxygen of TiO$_2$[16]. Next, the S 2p spectra of the catalyst was shown in Fig. 5c. A well symmetrical S 2p peak at binding energy 169.5 eV was observed, corresponding to S^{6+} state of SO$_4^{2-}$ species[31,32]. The binding energy at 164.6 eV was attributed to elemental sulfur[33], which was overlapped with Bi 4f XPS spectra. Hence, the SO$_4^{2-}$ species were mainly adsorbed on the catalyst surface, which improved surface acid strength and favored to the adsorption and degradation of the pollutants[22,34]. The Bi 4f XPS spectrum was shown in Fig. 5d. The peak at binding energy 159.5 eV was attributed to Bi 4$f_{7/2}$, while the peak at binding energy 164.7 eV belonged to Bi 4$f_{5/2}$. These values of binding energies were higher than the binding energy of Bi^{3+}, indicating that bismuth existed in Bi$^{3+\delta}$ state and formed Bi–O–Ti bond[16]. The intensities of Bi 4f
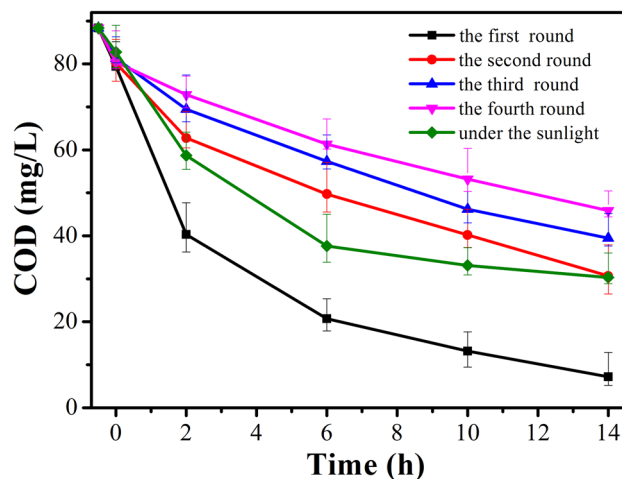
Figure 6.. COD_{Cr} change as a function of time in wastewater of recycle reactions using F–S–Bi–TiO_2/SiO_2 catalyst under natural sunlight irradiation.

peaks of F–S–Bi–TiO_2/SiO_2 were decreased as compared to F–S–Bi–TiO_2, which indicate that dispersion function of silica was selective, that was only favorable for the substitution of F for the lattice oxygen but not for the formation Bi oxides. The weight percentages of the elements in the F–S–Bi–TiO_2/SiO_2 and F–S–Bi–TiO_2 were shown in Table S2.

Photocatalytic purification of industrial acrylonitrile wastewater. On the basis of above analysis (Tables 1 and 2) we found that, there were a lot of inorganic and organic substances in the industrial acrylonitrile wastewater and these substances inhibited the catalyst activity (Fig. 1a). Specially, low ratio of BOD to COD_{Cr} (Table 2) identified that biochemical treatment could not be used. On the other hand, since there was limitation in amount of adsorption (Fig S1), the use of adsorption to treat was also hardly to reach regulation discharge. Hence, photocatalytic degradation of industrial acrylonitrile wastewater was one of most promising technique. A stable light source was required to keep experimental repeatability as mentioned in Table S1. Figure 6 shows the change in the value of COD_{Cr} as a function of illumination time under simulated sunlight. It was found that COD_{Cr} value decreased from 88.36 to 7.20 mgL^{-1} and TOC concentration decreased from 39.45 to 2.57 mgL^{-1} for 14 h irradiation. F–S–Bi–TiO_2/SiO_2 catalyst was recycled through filtration after reaction and the recovery ratio was more than 95%. The photocatalytic reaction performance of recycled F–S–Bi–TiO_2/SiO_2 was demonstrated through repeated rounds under the same reaction conditions. The value of COD_{Cr} was 30.67 mgL^{-1} after 14 h of illumination at the second round. After photocatalysis, the value of COD_{Cr} was 45.86 mgL^{-1} at the fourth round.

Figure 6 shows the photocatalytic activity of fresh F–S–Bi–TiO_2/SiO_2 catalyst for the degradation of pollutants in industrial acrylonitrile wastewater under natural sunlight irradiation. The value of COD_{Cr} decreased to 39 mgL^{-1} after 6 h irradiation, which has satisfied China national discharge standards.

Discussion

The actual textile dyeing wastewater was effectively oxidized by TiO_2 under UV radiation. The degradation percentage of the dye and COD_{Cr} were 98.50% and 91.50%, respectively[11]. Dai et al.[25] investigated the adsorption purification of acrylonitrile production wastewater by a microporous zeolite, CS-Z1 and a visible light-driven Ti–$β$–Bi_2O_3 photocatalyst. Nanoporous Ti–$β$–Bi_2O_3 was prepared via a solvothermal synthesis method in laboratory. Dai et al. was mainly interested in the theory, but not in application. They have not considered the inorganic ions effects. In this paper, we used industrial acrylonitrile wastewater as testing samples. The industrial acrylonitrile wastewater was pretreated by microporous zeolite, HZSM-5. After the treatment, the wastewater contained some inorganic and organic matter, as shown in Tables 1 and 2. Some of them were same or different to the pollutants reported by Dai et al. Table 2 only gives out a part of interfering inorganic ions And the existence of these ions could slow down the reaction rate (Fig. 1a). Our results showed that the prepared catalyst possesses certain anti-interfering ability. From the application point of view, we have used simple SiO_2 dispersing sol–gel for the synthesis of highly active ultrafine nanoparticle catalyst with certain anti-ion interfering function and for the first time we successfully degraded industrial acrylonitrile wastewater in only 6 h under natural sunlight. This is the most significant findings for the photocatalysis application in environment.

For most of the pollutants, close to zero discharge is a final goal that people pursue in environment protection. Sixto et al.[10] have demonstrated that photocatalytic purification of phenol containing wastewater by TiO_2-P25 using sacrificial agent under ultraviolet part of sunlight. In this study, there was not any sacrificial agent, however, we still realized that the values of COD_{Cr} and TOC near zero discharge. These results show the potential of as prepared photocatalyst in near zero discharge and high TOC removal efficiency of wastewater treatment.

In our previous study, we found that the reaction rate of the catalyst with SiO_2 was several times faster than without SiO_2. The later exhibited some general properties of a large bulk aggregate. On the other hand, there were a majority of ultrafine nanoparticles with acidic sites on the catalyst with SiO_2[20]. A large number of bumps increased the quantum size effect and UV absorption at 270–380 nm, which should raise activity. Several nanometers package of irregular crystal films have promotion effect on light absorption. Photon were generated by light which can go through several nanometers of irregular $Bi_4Ti_3O_{12}$ out layer film and get into TiO_2 (Fig. 2e), causes scattering at the rough interface of the both phases. Apparently, it should be favorable to light absorption and to promote the catalytic activity (Fig. 6). The bumps were different with films of packages in morphology, but we think that were consistent in functions, because their sizes were in approximate ranges of several nanometers (Fig. 2e, g). Apparently, there were much more F^- ion in the lattice, which could produce holes[19] and also contribute the high activity of the catalyst with silica dispersion.

Conclusion

We built up a most simple and low cost approach for the preparation of ultrafine nanocatalyst of F, S and Bi doped TiO_2 with SiO_2 dispersing sol–gel particles and successively degraded the organic pollutants in acrylonitrile industrial wastewater to reach national discharge standard under 6 h of natural sunlight irradiation. In the prepared photocatalyst the doping of F, S and Bi causes the enhanced absorbance in the visible region. The results of photocatalytic activity evaluation demonstrated that COD_{Cr} value reached to discharge standard still after four recycle uses under the simulated sunlight irradiation, and to near zero discharge for the fresh photocatalyst. These results exhibited effectiveness and potential of our photocatalyst for the treatment of complicated and refractory industrial wastewater. The XPS and EDS analysis implied that S and Bi were doped successfully. The photocatalyst size distribution has been identified by visible nano-aggregates, constructed with 2–4 nm of finer gel particles. It indicated the function of SiO_2 dispersing to form ultrafine nanoparticles. The nano-aggregates might form an identical lattice faces or different faces when gel particles crystallized. TEM results revealed that, the bump's numbers may also be responsible for the increase in the light adsorption and photocatalytic activity. The identical face might originate from silk ribbon film of package. The crystals of several nanometers of out layer films and rough core surfaces of packages also increased the light absorption and enhance their photocatalytic activity.

References

1. Ma, S. M. & Gu, P. Research progress in acrylonitrile wastewater treatment. *Ind. Water Treat.* **33**, 13–17 (2013).
2. Zheng, D. J. *et al.* Pilot-scale integrated membrane system for the treatment of acrylonitrile wastewater. *Desalination* **357**, 215–224 (2015).
3. Chu, Y. Y., Qian, Y. & Bai, M. J. Three advanced oxidation processes for the treatment of the wastewater from acrylonitrile production. *Water Sci. Technol.* **60**(11), 2991–2999 (2009).
4. Zheng, D. J. *et al.* Coagulation pretreatment of highly concentrated acrylonitrile wastewater from petrochemical plants. *Water Sci. Technol.* **70**(2), 345–351 (2014).
5. Yan, G. X., Cai, B., Chen, C. M., Wang, Q. H. & Guo, S. H. Biodegradability evaluation of pollutants in acrylonitrile wastewaters based on particle size distribution. *Desalin. Water Treat.* **53**(10), 2792–2798 (2015).
6. Yu, C. F. *et al.* One-pot fabrication of β-Bi_2O_3@Bi_2S_3 hierarchical hollow spheres with advanced sunlight photocatalytic RhB oxidation and Cr(VI) reduction activities. *Appl. Surf. Sci.* **455**(15), 8–17 (2018).
7. Yu, C. F. *et al.* One-pot facile synthesis of Bi_2S_3/SnS_2/Bi_2O_3 ternary heterojunction as advanced double Z-scheme photocatalytic system for efficient dye removal under sunlight irradiation. *Appl. Surf. Sci.* **420**(31), 233–242 (2017).
8. Yu, C. F. *et al.* Preparation and characterization of sphere-shaped $BiVO_4$/reduced graphene oxide photocatalyst for an augmented natural sunlight photocatalytic activity. *J. Alloys Compd.* **677**(25), 219–227 (2016).
9. Fujishima, A., Rao, T. N. & Tryk, D. A. Titanium dioxide photocatalysis. *J. Photochem. Photobiol. C.* **1**, 1–21 (2000).
10. Sixto, M. R., Christoph, R., Julián, B. G. & Martín, V. Photocatalytic degradation of industrial residual waters. *Sol. Energy.* **56**(5), 401–410 (1996).
11. Hosseini, S. M. B., Fallah, N. & Royaee, S. J. Optimization of photocatalytic degradation of real textile dye house wastewater by response surface methodology. *Water Sci. Technol.* **74**(9), 1999–2009 (2016).
12. Watanabe, T. *et al.* Photocatalytic activity and photoinduced hydrophilicity of titanium dioxide coated glass. *Thin Solid Films* **351**(1–2), 260–263 (1999).
13. Miguel, P. *et al.* A review on the visible light active titanium dioxide photocatalysts for environmental applications. *Appl. Catal. B Environ.* **125**(21), 331–349 (2012).
14. Deskins, N. A., Rousseau, R. & Dupuis, M. Defining the role of excess electrons in the surface chemistry of TiO_2. *J. Phys. Chem. C* **114**(15), 5891–5897 (2010).
15. Zhou, X. M., Liu, N. & Patrik, S. Photocatalysis with TiO_2 nanotubes: "colorful" reactivity and designing site-specific photocatalytic centers into TiO_2 nanotubes. *ACS Catal.* **7**, 3210–3235 (2017).
16. Reddy, P. A. K., Srinivas, B., Kala, P., Kumari, V. D. & Subrahmanyam, M. Preparation and characterization of Bi-doped TiO_2 and its solar photocatalytic activity for the degradation of isoproturon herbicide. *Mater. Res. Bull.* **46**(11), 1766–1771 (2011).
17. Li, D., Haneda, H., Labhsetwar, N. K., Hishita, S. & Ohashi, N. Visible-light-driven photocatalysis on fluorine-doped TiO_2 powders by the creation of surface oxygen vacancies. *Chem. Phys. Lett.* **401**(4–6), 579–584 (2005).
18. Li, D., Ohashi, N., Hishita, S., Kolodiazhnyi, T. & Haneda, H. Origin of visible-light-driven photocatalysis: a comparative study on N/F-doped and N–F-codoped TiO_2 powders by means of experimental characterizations and theoretical calculations. *J. Solid State Chem.* **178**(11), 3293–3302 (2005).
19. Akpan, U. G. & Hameed, B. H. Enhancement of the photocatalytic activity of TiO_2 by doping it with calcium ions. *J. Colloid Interface Sci.* **357**(1), 168–178 (2011).
20. Pang, D. D., Wang, Y. T., Ma, X. D. & Ouyang, F. Fluorine promoted and silica supported TiO_2 for photocatalytic decomposition of acrylonitrile under simulant solar light irradiation. *Chem. Eng. J.* **258**, 43–50 (2014).
21. Yu, J. C., Yu, J. G., Ho, W. K., Jiang, Z. T. & Zhang, L. Z. Effects of F doping on the photocatalytic activity and microstructures of nanocrystalline TiO_2 powders. *Chem. Mater.* **14**(9), 3808–3816 (2002).

22. Pang, D. D., Qiu, L., Zhu, R. S. & Ouyang, F. Silica supported SO_4^{2-}/TiO_2 for photocatalytic decomposition of acrylonitrile under simulant solar light irradiation. *Chem. Eng. J.* **270**, 590–596 (2015).
23. Samantaray, S. K., Mohapatra, P. & Parida, K. Physico-chemical characterization and photocatalytic activity of nanosized SO_4^{2-}/TiO_2 towards degradation of 4-nitrophenol. *J. Mol. Catal. A Chem.* **198**(1–2), 277–287 (2003).
24. Li, J. J. *et al.* Solvothermal syntheses of Bi and Zn co-doped TiO_2 with enhanced electron–hole separation and efficient photodegradation of gaseous toluene under visible-light. *J. Hazard. Mater.* **325**, 261–270 (2017).
25. Dai, Y. R., Song, Y. H., Tu, X., Jiang, Y. P. & Yuan, Y. Sequential shape-selective adsorption and photocatalytic transformation of acrylonitrile production wastewater. *Water Res.* **85**, 216–225 (2015).
26. Li, H. L. *et al.* Efficient photocatalytic degradation of acrylonitrile by sulfur-bismuth co-doped F–TiO_2/SiO_2 nanopowder. *Chemosphere* **249**, 126135 (2020).
27. Hisatomi, T. & Domen, K. Reaction systems for solar hydrogen production via water splitting with particulate semiconductor photocatalysts. *Nat. Catal.* **2**(5), 387–399 (2019).
28. Yu, C., Zhou, W., Yang, K. & Rong, G. Hydrothermal synthesis of hemisphere-like F-doped anatase TiO_2 with visible light photocatalytic activity. *J. Mater. Sci.* **45**(21), 5756–5761 (2010).
29. Wu, Y. M., Xing, M. Y., Tian, B. Z., Zhang, J. L. & Chen, F. Preparation of nitrogen and fluorine co-doped mesoporous TiO_2 microsphere and photodegradation of acid orange 7 under visible light. *Chem. Eng. J.* **162**(2), 710–717 (2010).
30. Yang, G. D. *et al.* Study on the photocatalysis of F–S co-doped TiO_2 prepared using solvothermal method. *Appl. Catal. B Environ.* **96**(3–4), 458–465 (2010).
31. Wu, Z. B., Jin, R. B., Wang, H. Q. & Liu, Y. Effect of ceria doping on SO_2 resistance of Mn/TiO_2 for selective catalytic reduction of NO with NH_3 at low temperature. *Catal. Commun.* **10**(6), 935–939 (2009).
32. Romano, E. J. & Schulz, K. H. A XPS investigation of SO_2 adsorption on ceria-zirconia mixed-metal oxides. *Appl. Surf. Sci.* **246**(1–3), 262–270 (2005).
33. Wei, F. Y., Ni, L. S. & Cui, P. Preparation and characterization of N–S-codoped TiO_2 photocatalyst and its photocatalytic activity. *J. Hazard. Mater.* **156**(1–3), 135–140 (2008).
34. Wang, X. C. *et al.* Probing of photocatalytic surface sites on SO_4^{2-}/TiO_2 solid acids by in situ FT-IR spectroscopy and pyridine adsorption. *J. Photochem. Photobiol. A Chem.* **179**(3), 339–347 (2006).

Acknowledgements

Author contributions

H.L.L., F.W.D., performed the experimental work and analyzed the results; L.Q. and F.Y.O. performed TEM and STEM measurement and analysis; F.Y.O., G.C. designed experiments and discussed the results; B.B. assisted in the GC–MS and XPS analysis; The paper was co-written by F.Y.O., L.Q., H.L.L., Z.Y.G., D.D.P. and Y.W.

Competing interests

The authors declare no competing interests.

Additional information

Supplementary information is available for this paper at https://doi.org/10.1038/s41598-020-69012-z.

Correspondence and requests for materials should be addressed to F.O. or L.Q.

Reprints and permissions information is available at www.nature.com/reprints.

Publisher's note Springer Nature remains neutral with regard to jurisdictional claims in published maps and institutional affiliations.